


Research Paper

Multi-Population African Vultures Optimized Fractional Derivative Virtual Inertia and Damping Control for Frequency Stabilization in Islanded Microgrid Network

S. Palaniyappan*  and M.M. Rajan Singaravel 

Department of Electrical and Electronics Engineering National Institute of Technology Puducherry, Karaikal, India.

Abstract— The growing integration of renewable energy sources (RESs) has reduced the rotational inertia of power grids, traditionally supplied by large rotating generators. This reduction makes grids more vulnerable to frequency variations. To address this challenge, this paper introduces a new fractional derivative virtual inertia and damping control (FDVIDC) strategy for enhancing frequency stability in an islanded microgrid (IMG) network. A fractional-order proportional integral derivative (FOPID) controller is employed to regulate the active power output in a biopower-dominated microgrid system. The parameters of both the FDVIDC and FOPID controllers are optimized using a new meta-heuristic algorithm called the Multi-population African Vultures Optimization (MAVO), with the integral time absolute error (ITAE) criterion as the performance index. The effectiveness of the proposed MAVO algorithm is demonstrated using standard benchmark test functions and is compared with the original African Vultures Optimization (AVO), Whale Optimization Algorithm (WOA), and Particle Swarm Optimization (PSO). Simulation results confirm that MAVO achieves a 90.74% reduction in ITAE, with a settling time of 9.573 seconds and a steady-state error of 2.809, indicating its superior convergence and control accuracy over PSO as the baseline. Time-domain analysis further confirms that the FOPID controller outperforms conventional PI and PID controllers. The robustness of the proposed control strategy is assessed under various operating scenarios. Finally, the proposed technique is validated through the OPAL-RT platform.

Keywords—Islanded microgrid, load frequency control, multi-population african vultures optimization, fractional derivative virtual inertia and damping control, renewable energy sources.

1. INTRODUCTION

Load frequency control (LFC) is a critical aspect of power system management, aimed at maintaining the balance between power production and consumption to keep the system frequency within acceptable limits. In traditional power system networks, large rotating generators provide inertia, helping to buffer sudden changes in demand or supply and maintain grid stability [1]. However, with the increasing integration of RESs, grid inertia is reduced, making the system more susceptible to frequency variations and instability. This reduction in inertia poses a critical challenge in IMG networks, where the grid operates independently from the main grid [2]. In such systems, maintaining frequency stability becomes more crucial due to the isolated nature of the grid. To address these challenges, virtual inertia (VI) is emerging as a promising solution to enhance frequency regulation of the IMG network [3].

Several studies have explored frequency control in low-inertia IMGs, mainly through energy storage systems (ESSs) enhanced

with VI support. One study [4] implemented the robust H_∞ technique to address virtual inertia control (VIC) challenges, effectively providing frequency support in low-inertia IMGs. Another study [5] analyzed the performance of a phase-locked loop (PLL) emulated VIC technique in the IMG networks. Model predictive control (MPC) was proposed in [6] to manage inertia power in the IMG system. At the same time, the coefficient diagram method (CDM) controller was introduced in [7] to demonstrate its ability to mimic frequency variations in IMG networks. Further, a study [8] presented a virtual inertia damping and control (VIDC) approach incorporating derivative control methods to stabilize frequency in small and large grid systems. An enhanced VIDC technique was proposed in [9] and [10], emulating VIDC to improve the system resilience. In [11], a new scaled sinusoidal arithmetic optimization method is used to fine-tune the control parameters of a multi-stage PID controller in the IMG system. Studies [12] and [13] explored the integration of a superconducting magnetic energy storage (SMES) unit, demonstrating improved performance in IMG networks. A novel virtual damping stabilizer for frequency stabilization in IMG systems was proposed in [14], while [15] introduced a VIDC strategy to enhance the LFC system. In the existing literature, thermal power plants with small capacities are used as base load units in combination with RESs. In contrast, this study proposes an IMG system powered by 100% RESs. To address the challenges associated with high-RES penetration, this paper introduces a novel VIDC strategy that incorporates a fractional derivative (FD) within the control loop. The proposed FDVIDC approach is specifically developed to enhance frequency stability in IMG networks with high-RES integration.

Received: 29 Apr. 2025

Revised: 28 Jun. 2025

Accepted: 09 Jul. 2025

*Corresponding author:

E-mail: eeepalani@gmail.com (S. Palaniyappan)

DOI: [10.22098/joape.2025.17332.2357](https://doi.org/10.22098/joape.2025.17332.2357)

This work is licensed under a [Creative Commons Attribution-NonCommercial 4.0 International License](https://creativecommons.org/licenses/by-nc/4.0/).

Copyright © 2025 University of Mohaghegh Ardabili.

Various optimization techniques are employed to fine-tune the controller parameters and the parameters of the VIDC technique. In [16], the mine blasting algorithm has been applied to tune a PI-TI controller for IMG networks, enhancing its frequency stability. The interval type-2 fuzzy logic PID (IT2FPID) controller parameters were tuned using optimization techniques such as the improved parasitism predation algorithm (IPPA) [17] and an equilibrium optimization algorithm [18] in the IMG network, providing precise control adjustments. The bird swarm algorithm (BSA) has also been utilized to optimize a 2DOF-TID controller for IMGs, ensuring better frequency regulation [19]. The reported literature has some limitations regarding convergence speed and global optimal solutions. This research addresses these gaps by introducing a novel optimization algorithm and a comprehensive control strategy designed for IMG networks with a significant presence of RESs.

Recently, new control methods have been developed for two-layer MPC [20], fuzzy logic control [21], synthetic inertia control [22], brain emotional learning controller [23], nonlinear MPC [24], and sliding mode controller [25] to improve frequency regulation in IMG systems. Despite these advancements, a gap remains in managing frequency regulation in IMG networks dominated by RESs. Therefore, there is a need for innovative approaches that can enhance frequency regulation and ensure grid stability in such systems. One promising approach involves using fractional order controllers (FOCs), which offer superior flexibility and performance in regulating active power output compared to traditional controllers [26]. Table 1 shows the comparative literature survey.

The motivation for LFC in a system lies in adapting to the evolving energy landscape. As the share of RESs continues to grow, developing and implementing effective control strategies is crucial for ensuring the stability and reliability of power systems. The decrease in inertia poses critical challenges for frequency regulation, where the system operates independently without the support of the main grid. Existing virtual inertia-based control methods have limitations such as conservative tuning, sensitivity to parameter variations, and lack of adaptability under high-RES penetration. To address these challenges, this study introduces an enhanced FDVIDC strategy integrated with an FOPID controller to improve the dynamic frequency response of RES-dominated IMG systems. As reported in the literature, various optimization techniques have been used to tune controller parameters. However, single-population metaheuristics often suffer premature convergence and stagnation. These issues are addressed by maintaining diversity through elite migration and the independent evolution of sub-populations. To overcome these limitations, a novel MAVO algorithm is proposed in this work. By optimizing the parameters of the FOPID and FDVIDC controllers, this research aims to enhance frequency regulation and ensure grid stability in 100% renewable energy-dominated IMG networks. The key contributions of this paper are as follows:

- 1) To develop a 100% RES-based IMG model that addresses the challenges of frequency regulation in fully renewable power systems.
- 2) To propose an MAVO-optimized FOPID controller that effectively suppresses frequency oscillations, demonstrating superior performance compared to conventional PI and PID controllers.
- 3) To validate the effectiveness of the MAVO technique by benchmarking it against well-known meta-heuristic algorithms, including PSO, WOA, and AVO under various dynamic operating conditions.
- 4) To verify the resilience of the designed control scheme, robustness testing is carried out by varying key parameters of the IMG system within a $\pm 25\%$ range. A comprehensive stability analysis is performed using eigenvalue plots to confirm the system's dynamic stability.
- 5) To confirm the real-time applicability of the proposed

approach through OPAL-RT simulations, demonstrating its practical viability for frequency control in IMG systems.

The remaining structure of this paper is summarized as follows: Section 2 delivers a comprehensive model of the IMG system. Section 3 explains the formulation and implementation of the FOPID controller. Section 4 details the proposed MAVO algorithm. Section 5 presents the simulation studies conducted to validate the performance of the proposed control strategy under different operating conditions. Finally, Section 6 summarizes the main conclusions and highlights the key contributions of the study.

2. MODELING OF THE IMG NETWORK

Fig. 1 presents the structural configuration of the IMG system integrated with the proposed FDVIDC strategy. The total generation capacity of the network is 1500 kW, comprising a 350 kW biomass-combined heat and power (BCHP), a 350 kW biodiesel engine generator (BDEG), a 350 kW biogas turbine generator (BGTG), and a 300 kW renewable energy (RE) micropower generator. Solar thermal power generation (STPG) and wind turbine power generation (WTPG) contribute to the RE micropower, supported by aqua electrolyzers (AE) and fuel cells (FC) functioning as energy storage components. To improve the system's inertial response and support frequency stability, a 150 kW hybrid energy storage (HES) system, consisting of battery energy storage (BES) and flywheel energy storage (FES), is employed. The proposed FDVIDC strategy is applied to effectively coordinate the HES units, enhancing inertia support and frequency regulation across the microgrid network.

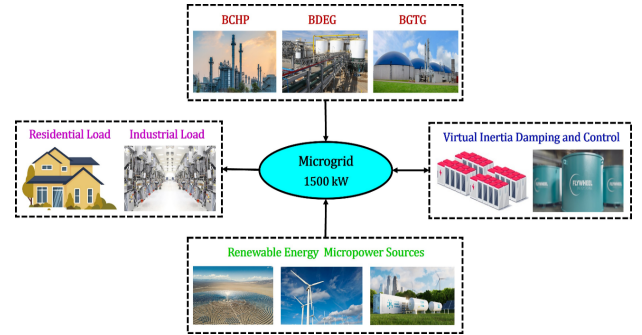


Fig. 1. Schematic configuration of IMG network.

Fig. 2 represents the block diagram of the proposed IMG network containing bioenergy sources, such as the BCHP, BDEG and BGTG units, as the base power generation for primary frequency regulation. Power fluctuations happen in the system because of sudden changes in load and the intermittent nature of RESs. As a result, these factors lead to frequency deviations in the IMG network, as stated in [27]:

$$\Delta f(s) = \frac{K_P}{1+sT_P} (\Delta P_{BCHP} + \Delta P_{BDEG} + \Delta P_{BGTG} + \Delta P_{RE} + \Delta P_{FDVIDC} - \Delta P_L) \quad (1)$$

The equation above represents the relationship between frequency deviation (Δf) and the factors influencing it, such as load changes and RES power fluctuations. This mathematical formulation is fundamental for analyzing system dynamics and designing appropriate control strategies.

2.1. Bioenergy sources

The IMG network utilizes BCHP, BDEG and BGTG plants as bioenergy sources. These plants are modeled using first-order transfer functions given below [27], [28].

Table 1. Comparative literature survey.

| Ref. | Type of controller / optimization | VI technique | Limitations of the reported algorithm | Advantages of the proposed MAVO algorithm |
|--------------------------------------|--|-------------------------|--|---|
| [4] | Robust H ∞ -based virtual synchronous generator (VSG) | VSG | (i) High computational complexity. (ii) Conservative performance. | (i) Lower complexity with MAVO tuning. (ii) Adaptive robustness. |
| [5] | H ∞ controller | PLL-based VIC | (i) Sensitive to measurement noise. (ii) No optimization framework. | (i) Noise-resilient tuning. (ii) MAVO optimizes for dynamic conditions. |
| [6] | MPC | MPC-based VIC | (i) Computationally intensive. (ii) Unsuitable for real-time systems. | (i) Faster convergence. (ii) MAVO reduces computational burden. |
| [7] | CDM | CDM-based VIC | (i) Limited to small-scale systems. (ii) Fixed parameters. | (i) Scalable for multi-microgrids. (ii) Dynamic parameter tuning. |
| [8] | Mixed-sensitivity H ∞ controller | VIDC | (i) Conservative tuning. (ii) Lacks adaptability to RES variability. | (i) Adaptive FDVIDC. (ii) MAVO optimizes for RES fluctuations. |
| [11] | Multi-stage PID controller / Sine-augmented scaled AOA | PLL-based VIC | (i) Uses integer-order PID. (ii) Lacks diversity. (iii) Poor handling of multimodal functions. | (i) Avoids local optima. (ii) MAVO employs FOPID + FDVIDC with strong exploration-exploitation balance. |
| [13] | PI controller / AVO algorithm | SMES-integrated VIC | (i) Single population. (ii) Premature convergence. (iii) Lacks resilience. | (i) MAVO overcomes AVO limitations via elite migration and multi-population diversity. |
| [17] | IT2FPIID controller / IPPA algorithm | PLL-based VIC | (i) Complex fuzzy rule base. (ii) No hardware validation. | (i) MAVO offers simpler design. (ii) High accuracy validated via OPAL-RT. |
| [18] | Type-2 FLC and FOPI / Equilibrium Optimization | VIC | (i) High tuning complexity due to fuzzy logic. (ii) Slower convergence. | (i) MAVO avoids fuzzy rules, ensures fast convergence and easier implementation. |
| [19] | 2DOF-TID controller / BSA algorithm | PLL-based VIC | (i) Inefficient in multimodal function tuning. (ii) Lacks damping consideration. | (i) MAVO accurately tunes FDVIDC + FOPID with elite sharing for robust search. |
| [21] | Fuzzy logic – rule based | VIC | (i) Rule dependency affects scalability. (ii) Less adaptable. | (i) MAVO is model-based, robust under varied scenarios and parameter shifts. |
| Proposed IMG work (100% RESs) | FOPID controller / MAVO algorithm | FDVIDC technique | – | (i) Multiple sub-populations for strong search diversity. (ii) Elite-solution sharing to avoid local minima. (iii) Balanced exploration and exploitation. (iv) Prevents premature convergence and suits high-dimensional optimization tasks. |

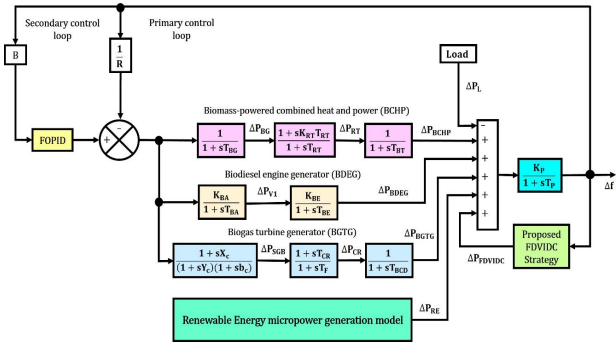


Fig. 2. Block diagram of IMG network.

$$\Delta P_{BCHP} = \left(\frac{1}{1+sT_{BG}} \right) \left(\frac{1+sK_{RT}T_{RT}}{1+sT_{RT}} \right) \left(\frac{1}{1+sT_{BT}} \right) \quad (2)$$

$$\Delta P_{BDEG} = \left(\frac{K_{BA}}{1+sT_{BA}} \right) \left(\frac{K_{BE}}{1+sT_{BE}} \right) \quad (3)$$

$$\Delta P_{BGTG} = \left(\frac{1+sX_C}{(1+sY_C)(1+sb_C)} \right) \left(\frac{1+sT_{CR}}{1+sT_F} \right) \left(\frac{1}{1+sT_{BCD}} \right) \quad (4)$$

2.2. RE micropower generation sources

STPG and WTPG plants are integrated into this network as RE micropower generation sources. The plants are modeled using transfer functions described as follows [29]:

$$G_{STPG}(s) = \frac{\Delta P_{STPG}}{\Delta P_{solar}} = \left(\frac{K_S}{1+sT_S} \right) \left(\frac{K_T}{1+sT_T} \right) \quad (5)$$

$$G_{WTPG}(s) = \frac{\Delta P_{WTPG}}{\Delta P_{wind}} = \frac{K_{WTG}}{1+sT_{WTG}} \quad (6)$$

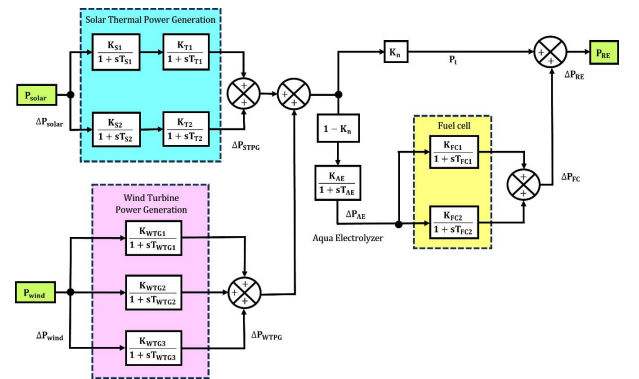


Fig. 3. Schematic diagram of RE micropower generation.

Fig. 3 shows the schematic diagram of RE micropower generation. The AE and FC are incorporated into the IMG network to regulate power fluctuations caused by RE micropower sources. The generalized transfer function models are given by [30]:

$$G_{AE}(s) = \frac{K_{AE}}{1+sT_{AE}} = \frac{\Delta P_{AE}}{(\Delta P_{STPG} + \Delta P_{WTPG})(1-K_n)} \quad (7)$$

$$K_n = \frac{P_t}{P_{STPG} + P_{WTPG}} \quad (8)$$

$$G_{FC}(s) = \frac{K_{FC}}{1 + sT_{FC}} \quad (9)$$

2.3. Proposed FDVIDC strategy

In traditional power system networks, synchronous generators provide physical inertia, which helps to stabilize frequency fluctuations caused by changes in load or generation. However, RESs lack this inherent inertia, making frequency control more challenging. Fig. 4 demonstrates that the conventional VIC technique for replicating rotating inertia uses a derivative method. This approach involves supplying energy from the inverter-based ESS to the grid whenever unexpected disruptions or contingencies occur. This method helps to stabilize the grid by quickly responding to changes and maintaining frequency balance [5], [7]. The dynamic model of the conventional VIC technique is denoted as follows:

$$\Delta P_{VIC} = \left[sH_V \left(\frac{1}{1 + sT_{ESS}} \right) \right] (\Delta f) \quad (10)$$

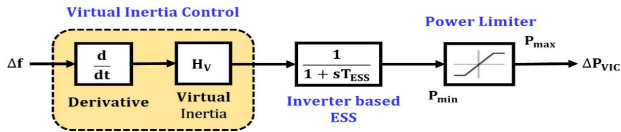


Fig. 4. Conventional VIC technique.

Virtual damping is not considered in the conventional VIC technique. So, the VIDC strategy is discussed in the previous literature [8–11] for injecting both inertia and damping to enhance stability and resilience while reducing frequency deviations. Fig. 5 represents the conventional VIDC strategy. The dynamic model is denoted as follows:

$$\Delta P_{VIDC} = \left[(sH_V + D_V) \left(\frac{1}{1 + sT_{ESS}} \right) \right] \Delta f \quad (11)$$

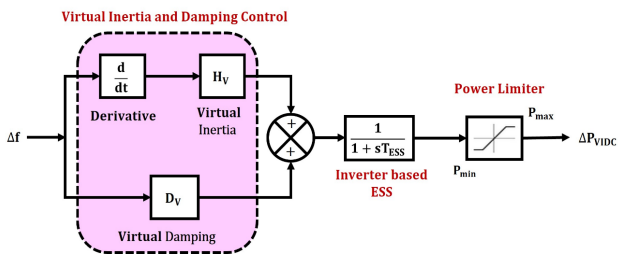


Fig. 5. Conventional VIDC strategy.

In this context, a new FDVIDC strategy is introduced in this study to provide instant inertia and damping into the IMG system. This FDVIDC operates independently from the conventional primary (droop) and secondary control loops, ensuring a dedicated focus on improving the IMG's dynamic performance. Fig. 6 provides a detailed overview of the proposed FDVIDC strategy implemented in the IMG network. The dynamic equation of the proposed FDVIDC scheme can be represented as follows:

$$\Delta P_{FDVIDC} = (s^\mu H_V + D_V) \left[\frac{K_{BES}}{1 + sT_{BES}} \cdot \frac{K_{FES}}{1 + sT_{FES}} \right] \Delta f \quad (12)$$

where, H_V , D_V , and s^μ are the virtual inertia, damping, and fractional derivative parameters of the FDVIDC controller.

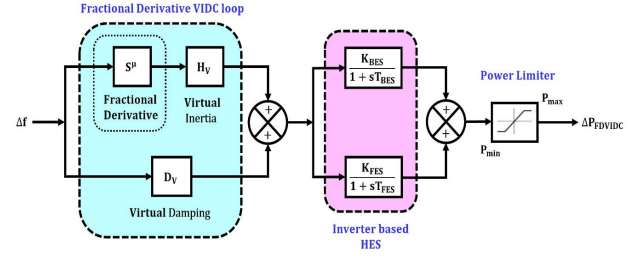


Fig. 6. Proposed FDVIDC scheme.

3. CONTROL APPROACH AND THE PROBLEM STATEMENT

Traditional PID controllers rely on integer-order derivatives and integrals, which may not offer the fine-tuning capabilities required for optimal performance in dynamic and complex microgrid environments. This can lead to suboptimal frequency regulation, particularly in systems with varying load conditions and disturbances. In contrast, FOPID controllers leverage fractional calculus to adjust the order of the proportional, integral, and derivative actions, providing greater flexibility and precision. This enables more accurate control and improved system stability, making FOPID controllers better suited for managing the intricate balance of load and generation in islanded microgrids. Fig. 7 displays the structure of FOPID controller. The FOPID controller can be stated as follows [28]:

$$u(t) = K_P + \frac{K_I}{s^\lambda} + K_D s^\mu \quad (13)$$

where, K_P , K_I , and K_D are the proportional, integral, and derivative gain parameters, and λ and μ are the fractional order operators.

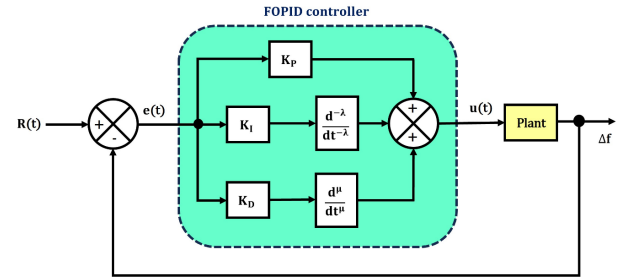


Fig. 7. Structure of FOPID controller.

The area control error (ACE) in an IMG network measures the deviation between actual and scheduled power levels, impacting frequency regulation. Proper ACE management ensures timely adjustments in the generation, minimizing frequency deviations and maintaining system stability. The ACE is represented as follows [31]:

$$ACE = B \Delta f \quad (14)$$

In this study, ITAE is selected as the objective function for tuning the parameters of the FDVIDC and FOPID controllers by minimizing ACE. It delivers better performance by reducing the settling time, control effort, and undershoots of the system compared to other steady-state indices. The objective function (J_{ITAE}) is represented as follows [27]:

$$ITAE = \min(J_{ITAE}) = \int_0^{t_s} t (|ACE| + |\Delta P_{FDVIDC}|) dt \quad (15)$$

Subjected to the following constraints:

$$\begin{aligned}
 K_P^{\min} &\leq K_P \leq K_P^{\max} \\
 K_I^{\min} &\leq K_I \leq K_I^{\max} \\
 \lambda^{\min} &\leq \lambda \leq \lambda^{\max} \\
 K_D^{\min} &\leq K_D \leq K_D^{\max} \\
 \mu^{\min} &\leq \mu \leq \mu^{\max} \\
 H_V^{\min} &\leq H_V \leq H_V^{\max} \\
 D_V^{\min} &\leq D_V \leq D_V^{\max} \\
 F_d^{\min} &\leq F_d \leq F_d^{\max}
 \end{aligned} \tag{16}$$

Where, t_s is the simulation time. To optimize the parameters of the FDVIDC strategy and determine the gain parameters of the FOPID controller, an appropriate meta-heuristic algorithm is required. This ensures the stable and efficient control of the IMG system.

4. MULTI-POPULATION AFRICAN VULTURES OPTIMIZATION TECHNIQUE

The AVO algorithm is structured to maintain a balance exploration and exploitation [32]. Despite its innovative design, the AVO has several limitations when addressing complex and dynamic optimization problems. Firstly, AVO tends to converge prematurely to suboptimal solutions in high-dimensional or multi-modal landscapes due to a lack of population diversity over iterations. This is particularly noticeable in late optimization stages, where most individuals crowd near the best-found solutions. Secondly, the exploitation mechanisms in AVO, although enhanced by multiple strategies (e.g., rotating flight and siege-flight), may lose efficiency in maintaining a proper balance between local refinement and global search, especially when the starvation control parameter F does not fluctuate dynamically enough. Furthermore, its single-population approach may lead to stagnation, where all vultures start behaving similarly, reducing the exploratory strength and adaptability in diverse search environments.

To address these challenges, the “multi-population” introduces a parallel evolutionary framework [33]. Instead of relying on a single group of vultures, multi-population uses multiple sub-populations that evolve independently, each exploring different regions of the search space. This multi-population setup maintains diversity and mitigates premature convergence by enabling isolated search paths. Periodic migration and elite solution sharing between populations foster knowledge transfer and help weaker sub-populations escape local minima. Each sub-population can also adopt unique configurations of exploitation and exploration strategies, making the overall algorithm more flexible and adaptive. The resulting hybrid behavior not only increases global convergence speed but also strengthens robustness against local optima, making MAVO a more efficient and scalable algorithm for frequency regulation in IMG systems. Fig. 8 presents the flowchart of the proposed MAVO algorithm. The step-by-step procedure and pseudo code for the MAVO algorithm is introduced in this section.

Step-1: Initialization

Define parameters: Number of sub-populations (P), number of vultures per population (N), Dimensions of solution vector (D), and Maximum number of iterations (T_{max}). Randomly initialize each vulture's position:

$$\begin{aligned}
 x_{i,j}^{(p)} &= lb_j + \text{rand.}(ub_j - lb_j) \\
 \text{for } i &= 1, \dots, N, j = 1, \dots, D, p = 1, \dots, P
 \end{aligned} \tag{17}$$

Step-2: Fitness evaluation

$$f(x_i^{(p)}) = \text{Objective Function}(x_i^{(p)}) \tag{18}$$

Step-3: Sub-population best identification

To determine the top two vultures per population using roulette-based selection.

$$p_i = \frac{F_i}{\sum_{j=1}^N F_j} \tag{19}$$

$$\begin{aligned}
 R(i) &= \\
 \begin{cases} \text{Best Vulture}_1^{(p)} & \text{if rand} < L_1 \\ \text{Best Vulture}_2^{(p)} & \text{otherwise} \end{cases}
 \end{aligned} \tag{20}$$

Step-4: Starvation rate computation

$$t = h \left[\sin \left(\frac{\omega \pi}{2} \frac{i}{T_{max}} \right) + \cos \left(\frac{\pi}{2} \frac{i}{T_{max}} \right) - 1 \right] \tag{21}$$

$$F = (2 \text{rand}_1 + 1) z \left(1 - \frac{i}{T_{max}} \right) + t \tag{22}$$

Step-5: Position update strategy

If $|F| \geq 1$: Exploration strategy (Global search)

Use either:

$$P(i+1) = R(i) - |X R(i) - P(i)| F \tag{23}$$

(or)

$$P(i+1) = R(i) - F + \text{rand}((ub - lb) \text{rand} + lb) \tag{24}$$

If $|F| \geq 0.5$: Exploitation strategy (Local search)

Use rotating flight:

$$S_1 = R(i) \left(\frac{\text{rand } P(i)}{2\pi} \right) \cos(P(i)) \tag{25}$$

$$S_2 = R(i) \left(\frac{\text{rand } P(i)}{2\pi} \right) \sin(P(i)) \tag{26}$$

$$P(i+1) = R(i) - (S_1 + S_2) \tag{27}$$

Or aggressive flight:

$$P(i+1) = R(i) - |d(t)| F \text{Levy}(d) \tag{28}$$

Step-6: Migration between populations

Every T_{mig} iterations:

$$x_j^{(p)} \leftarrow x_{\text{best}}^{(q)} + \delta \left(x_{\text{best}}^{(p)} - x_{\text{best}}^{(q)} \right) \tag{29}$$

Where, δ is a small random coefficient and $p \neq q$.

Step-7: Global best update

Track and update the best solution across all populations.

Step-8: Termination

Repeat steps 3 to 7 until the maximum iteration count T_{max} is reached.

Pseudo code for MAVO algorithm

```

1  Input: P, N, D, Tmax, Objective Function
2  Output: Global best solution
3  Initialization: Initialize P sub-populations randomly
4  Evaluate the fitness of each vulture; Identify BestVulture1 and BestVulture2
5  while iteration i < Tmax
6    for each population p
7      for each vulture i
8        Compute starvation rate F
9        if |F| ≥ 1
10         Perform exploration using Eq. (23) or Eq. (24) [32]
11       else if |F| ≥ 0.5
12         Apply exploitation using Eq. (27) [32]
13       else
14         Perform deep exploitation using Eq. (28) [32]
15       End
16       if mod (iteration, Tmig) = 0
17         Exchange best solutions between sub-populations [33]
18       End
19       Update global best solution
20     End
21   End
22 End while
23 Return global best solution

```

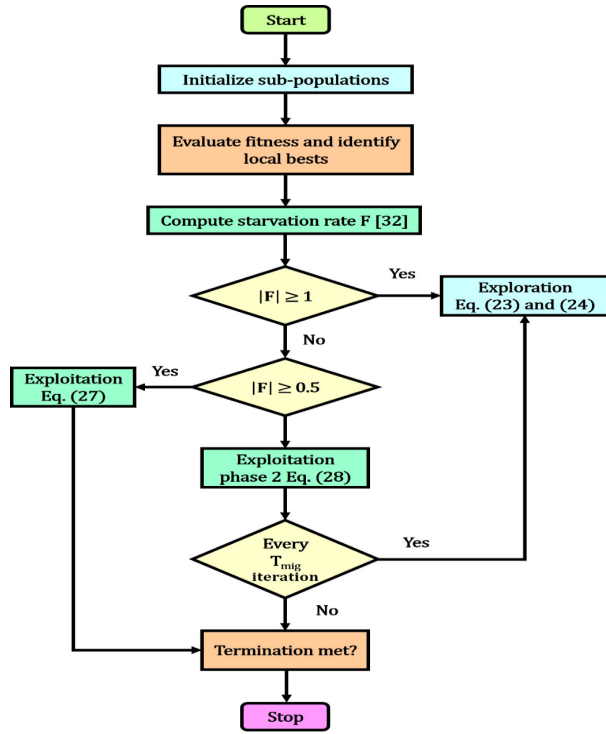


Fig. 8. MAVO flow chart.

5. SIMULATION RESULTS AND DISCUSSION

The performance of the newly proposed MAVO technique is assessed by comparing it with standard optimization algorithms such as PSO, WOA, and original AVO using established benchmark functions. Additionally, the MAVO-tuned FOPID controller is analyzed within the context of the IMG network. The parameters used for the IMGs in the simulations are detailed in Appendix A, and the results have been obtained accordingly.

5.1. Benchmark testing

A set of twenty-three benchmark functions is used to evaluate the performance of the proposed MAVO algorithm. Here, F1 to F7 are unimodal, featuring a single global optimum, and are used to assess exploitation capabilities. Functions F8 to F23 are classified as multimodal, featuring numerous global optima, and are employed to evaluate the exploration capabilities of optimization algorithms. The effectiveness of the proposed MAVO technique is evaluated using various performance indices, including the best, mean, and standard deviation (SD) values. Table 2 provides the performance evaluation results of these benchmark functions based on 25 independent trial runs.

The numerical results in Table 2 reveal that the MAVO algorithm effectively minimizes the fitness (objective) function value than PSO, WOA, and original AVO. Additionally, the lower SD indicates that MAVO exhibits the highest consistency across all benchmark functions. The tuning of the proposed FDVIDC and FOPID controller parameters using different optimization algorithms is detailed in Table 3.

5.2. Computational analysis

Fig. 9 depicts the convergence performance of the proposed MAVO algorithm, which is compared with AVO, WOA, and PSO. The curves show that MAVO reaches the optimal solution faster and with fewer iterations. Its curve drops sharply in the early stages and stabilizes quickly, indicating better convergence speed and accuracy. Unlike the other algorithms, MAVO avoids getting stuck in local optima and maintains consistent improvement throughout the process. This proves that MAVO is more efficient and reliable for tuning the FOPID controller in the IMG system.

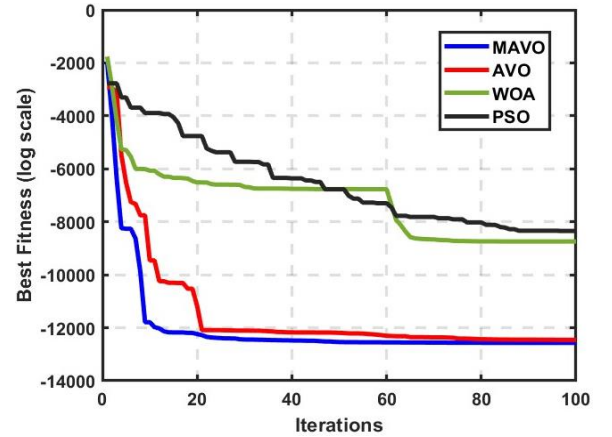


Fig. 9. Convergence curve.

The tuning limits for the control parameters of the FOPID and FDVIDC strategies are predefined with upper and lower bounds. These boundaries are selected to maintain system stability while ensuring optimal control performance. For FOPID, K_P , K_I , and K_D are limited to $[-100, -0.01]$, while λ and μ are confined to $[0, 1]$. For FDVIDC, the virtual inertia (H_V) ranges from 0 to 5, the damping constant (D_V) ranges from 0 to 5 and the fractional derivative constant (F_d) ranges from 0 to 1.

5.3. Time-domain analysis of the IMG network

The performance of the MAVO-tuned FOPID controller, combined with the proposed FDVIDC scheme within the IMG system, is verified through detailed time-domain simulations. Multiple operating scenarios are examined, including step load perturbation (SLP), random load perturbation (RLP), variations in RESS, and a comparative evaluation of the FDVIDC approach against earlier VIC methods to comprehensively assess the system's dynamic behavior.

Table 2. Performance assessment along with its statistical results.

| Fun | Cat | Index | PSO | WOA | AVO | MAVO |
|-----|-----|-------|------------|------------|------------|------------|
| F1 | US | Best | 1.9424e3 | 9.7639e-15 | 4.3616e-67 | 1.3793e-97 |
| | | SD | 5.2141e3 | 7.6861e-12 | 4.0871e-43 | 1.9668e-73 |
| | | Mean | 6.8905e3 | 5.2995e-12 | 9.1391e-44 | 4.4002e-74 |
| F2 | UN | Best | 5.5502e1 | 3.0513e-11 | 5.1221e-35 | 2.6339e-50 |
| | | SD | 1.9337e3 | 1.2149e-8 | 1.6528e-24 | 1.1336e-38 |
| | | Mean | 5.2369e2 | 5.5741e-9 | 5.2080e-25 | 4.7243e-39 |
| F3 | UN | Best | 2.9388e4 | 3.0965e4 | 3.6371e-57 | 1.2274e-76 |
| | | SD | 9.0731e3 | 2.6999e4 | 3.9842e-28 | 1.0087e-46 |
| | | Mean | 4.3102e4 | 9.4763e4 | 8.9620e-29 | 2.2573e-47 |
| F4 | US | Best | 4.1915e1 | 1.1668e1 | 3.7348e-34 | 1.5659e-49 |
| | | SD | 8.0357e0 | 2.6053e1 | 2.7150e-21 | 8.4365e-36 |
| | | Mean | 5.4030e1 | 6.2908e1 | 6.1282e-22 | 1.9032e-36 |
| F5 | UN | Best | 5.4676e5 | 2.8698e1 | 6.1512e-5 | 3.3564e-5 |
| | | SD | 1.8371e6 | 4.0260e-2 | 1.9142e-2 | 7.2200e-4 |
| | | Mean | 2.9999e6 | 2.8798e1 | 1.4553e-2 | 7.6406e-4 |
| F6 | US | Best | 3.3020e3 | 8.7394e-1 | 1.4505e-4 | 2.8712e-6 |
| | | SD | 4.6175e3 | 5.7170e-1 | 1.1349e-1 | 4.0795e-5 |
| | | Mean | 7.9318e3 | 2.0393e0 | 5.9050e-2 | 5.2245e-5 |
| F7 | US | Best | 1.2434e0 | 1.1914e-3 | 3.0893e-5 | 7.8997e-6 |
| | | SD | 5.8355e0 | 1.5000e-2 | 9.6696e-4 | 1.7979e-4 |
| | | Mean | 6.0464e0 | 2.2200e-2 | 1.1077e-3 | 1.8572e-4 |
| F8 | MS | Best | -9.7981e3 | -1.2534e4 | -1.2569e4 | -1.2569e4 |
| | | SD | 7.4033e2 | 1.1495e3 | 1.6946e3 | 4.0447e2 |
| | | Mean | -7.9599e3 | -8.9374e3 | -1.1455e4 | -1.2318e4 |
| F9 | MS | Best | 1.9948e2 | 5.6843e-14 | 0 | 0 |
| | | SD | 3.6540e1 | 1.2748e1 | 0 | 0 |
| | | Mean | 2.6497e2 | 3.267e0 | 0 | 0 |
| F10 | MN | Best | 1.1425e1 | 5.7091e-9 | 4.4409e-16 | 4.4409e-16 |
| | | SD | 2.9133e0 | 8.5025e-7 | 0 | 0 |
| | | Mean | 1.6370e1 | 6.4751e-7 | 4.4409e-16 | 4.4409e-16 |
| F11 | MN | Best | 2.2651e1 | 5.7732e-15 | 0 | 0 |
| | | SD | 3.2747e1 | 1.8086e-1 | 0 | 0 |
| | | Mean | 5.2704e1 | 4.0441e-2 | 0 | 0 |
| F12 | MN | Best | 1.9096e4 | 2.7265e-2 | 3.2603e-6 | 2.8187e-8 |
| | | SD | 1.0570e6 | 9.5274e-2 | 3.1535e-3 | 3.0019e-7 |
| | | Mean | 1.1664e6 | 1.5101e-1 | 1.6997e-3 | 3.7543e-7 |
| F13 | MN | Best | 2.5097e6 | 1.9339e-1 | 8.0740e-7 | 2.0832e-7 |
| | | SD | 4.9237e6 | 4.0165e-1 | 3.7232e-4 | 6.3041e-7 |
| | | Mean | 7.2643e6 | 1.0758e0 | 1.3163e-4 | 1.1945e-5 |
| F14 | FM | Best | 9.9810e-1 | 9.9810e-1 | 9.9810e-1 | 9.9810e-1 |
| | | SD | 4.4366e-1 | 3.8315e0 | 3.0144e0 | 5.1931e-1 |
| | | Mean | 1.0972e0 | 4.6292e0 | 3.1127e0 | 1.1966e0 |
| F15 | FM | Best | 6.7200e-4 | 3.4607e-4 | 3.0838e-4 | 3.0944e-4 |
| | | SD | 9.3765e-3 | 3.4849e-3 | 1.9712e-3 | 2.3112e-4 |
| | | Mean | 7.9216e-3 | 1.8194e-3 | 1.1332e-3 | 5.2064e-4 |
| F16 | FM | Best | -1.0318e0 | -1.0318e0 | -1.0318e0 | -1.0318e0 |
| | | SD | 2.8580e-8 | 1.3537e-6 | 6.9039e-11 | 8.8232e-17 |
| | | Mean | -1.0318e0 | -1.0318e0 | -1.0318e0 | -1.0318e0 |
| F17 | FM | Best | 3.9792e-1 | 3.9792e-1 | 3.9792e-1 | 3.9792e-1 |
| | | SD | 2.3387e-10 | 1.2895e-2 | 3.0853e-11 | 3.9786e-16 |
| | | Mean | 3.9792e-1 | 4.0137e-1 | 3.9792e-1 | 3.9792e-1 |
| F18 | FM | Best | 3.0010e0 | 3.0010e0 | 3.0010e0 | 3.0010e0 |
| | | SD | 1.2347e-8 | 8.3646e0 | 7.9443e-4 | 1.9354e-6 |
| | | Mean | 3.0010e0 | 5.7181e0 | 3.0003e0 | 3.0010e0 |
| F19 | FM | Best | -3.8638e0 | -3.8638e0 | -3.8638e0 | -3.8638e0 |
| | | SD | 7.7694e-2 | 5.0882e-2 | 6.1145e-4 | 1.7925e-13 |
| | | Mean | -3.8446e0 | -3.8281e0 | -3.8626e0 | -3.8638e0 |
| F20 | FM | Best | -3.3221e0 | -3.3192e0 | -3.3221e0 | -3.3221e0 |
| | | SD | 8.8618e-2 | 1.1370e-1 | 6.0167e-2 | 6.0686e-2 |
| | | Mean | -3.1989e0 | -3.1388e0 | -3.2701e0 | -3.2566e0 |
| F21 | FM | Best | -1.0155e1 | -1.0086e1 | -1.0155e1 | -1.0155e1 |
| | | SD | 3.2813e0 | 2.4844e0 | 5.1196e-7 | 2.1913e-11 |
| | | Mean | -6.7578e0 | -7.0698e0 | -1.0155e1 | -1.0155e1 |
| F22 | FM | Best | -1.0413e1 | -1.0352e1 | -1.0413e1 | -1.0413e1 |
| | | SD | 3.1949e0 | 3.2568e0 | 4.1134e-7 | 2.9347e-11 |
| | | Mean | -5.8589e0 | -6.7143e0 | -1.0406e1 | -1.0406e1 |
| F23 | FM | Best | -1.0538e1 | -1.0394e1 | -1.0538e1 | -1.0538e1 |
| | | SD | 3.8461e0 | 3.1844e0 | 2.7653e-7 | 5.1004e-11 |
| | | Mean | -5.7580e0 | -6.1174e0 | -1.0537e1 | -1.0537e1 |

A) Performance evaluation of the proposed FDVIDC strategy for SLP condition (Scenario-1)

All RESs are essential to meet the power requirement with a specified SLP of 0.2 p.u. (300 kW) at $t=0$ s. It ensures intermittent sources such as SPV and WTPG maintain consistency within the IMG system. Fig. 10 illustrates the change in frequency curve of the IMG network, utilizing the FOPID controller optimized

Table 3. Controller gains optimized by various algorithms.

| Different optimization | FDVIDC | | | FOPID | | | | |
|------------------------|--------|-------|----------------|----------------|----------------|-----------|----------------|-------|
| | HV | DV | F _d | K _P | K _I | λ | K _D | μ |
| PSO | 0.489 | 0.243 | 0.009 | -20.026 | -42.485 | 0.968 | -5.866 | 0.999 |
| WOA | 1.977 | 0.221 | 0.007 | -40.092 | -45.849 | 0.916 | -12.993 | 0.998 |
| AVO | 2.299 | 0.301 | 0.006 | -49.919 | -56.189 | 0.905 | -13.779 | 0.992 |
| MAVO | 0.696 | 2.045 | 0.004 | -50.806 | -59.302 | 0.884 | -14.519 | 0.986 |

through various algorithms, including MAVO, AVO, WOA, and PSO.

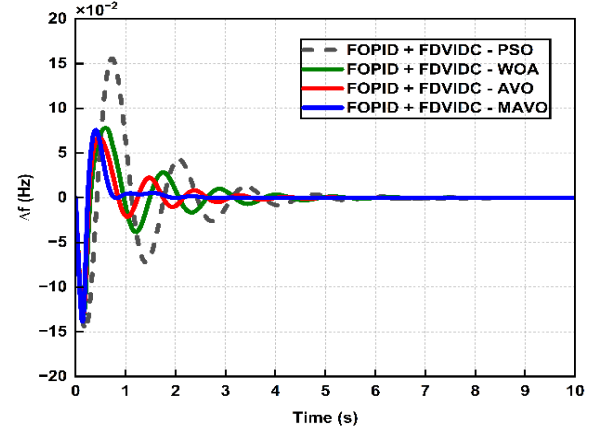


Fig. 10. System frequency response of the IMG with different algorithms (Scenario-1).

Compared to previous algorithms, the MAVO-tuned FOPID dampens frequency deviation quickly. The suggested MAVO technique has claimed to outperform other FOPID controller-based optimization approaches. Table 4 details the transient performance parameters of the FOPID controller tuned by different optimization approaches in this case. The data demonstrate that the MAVO algorithm excels in settling time, overshoot, control effort, undershoot, and other metrics.

Table 4. Assessment of transient responses of different algorithms (Scenario-1).

| Transient parameters | PSO-FOPID | WOA-FOPID | AVO-FOPID | MAVO-FOPID |
|---------------------------------------|-----------|-----------|-----------|------------|
| T_R (s) ($\times 10^{-5}$) | 3.709 | 3.289 | 2.957 | 2.905 |
| T_P (s) | 4.894 | 4.624 | 3.336 | 1.758 |
| T_S (s) | 9.998 | 9.996 | 9.981 | 9.573 |
| T_P (s) ($\times 10^{-1}$) | 7.162 | 1.557 | 1.453 | 1.383 |
| SSE ($\times 10^{-5}$) | 4.388 | 3.149 | 3.038 | 2.809 |
| CE (J) ($\times 10^{-1}$) | -0.058 | -0.042 | -0.051 | -0.049 |
| ITAE | 0.227 | 0.109 | 0.058 | 0.021 |
| ITSE ($\times 10^{-2}$) | 1.167 | 0.279 | 0.137 | 0.081 |
| IAE ($\times 10^{-1}$) | 1.799 | 0.957 | 0.682 | 0.461 |
| ISE ($\times 10^{-2}$) | 1.545 | 0.513 | 0.373 | 0.330 |
| $ P - O $ (p.u.) ($\times 10^{-1}$) | 1.555 | 0.780 | 0.775 | 0.759 |
| $ P - U $ (p.u.) | -0.128 | -0.132 | -0.134 | -0.139 |

The proposed MAVO-FOPID controller achieved the objective function ITAE value of 0.021. This demonstrates superior performance in comparison with other methods, with the ITAE being 90.74% lower than the value obtained using PSO, 80.73% lower than WOA, and 63.79% lower than AVO. Moreover, additional performance indices such as the ITSE, IAE, and ISE are reported in Table 4. The MAVO-optimized values exhibit superior performance, yielding lower values than the other three algorithms. The performance of the IMG network is further analyzed using the gain parameters of different controllers, which have been optimized through the MAVO algorithm, as illustrated in Fig. 11. The results indicate that the MAVO-optimized FOPID controller outperforms the other controllers in terms of control efficiency.

Table 5 shows the transient response parameter values of the controllers (PI, PID, and FOPID) optimized with the MAVO

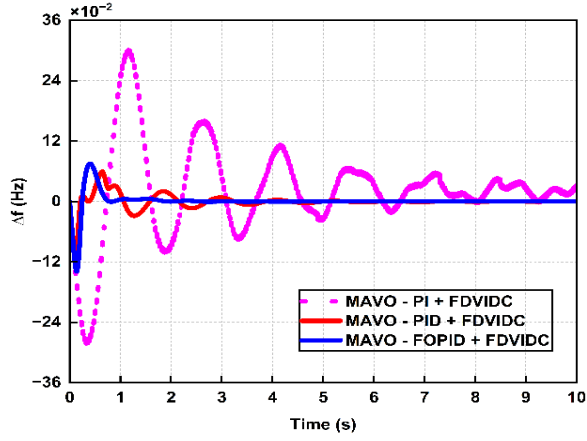


Fig. 11. System frequency response of the IMG with different controllers (Scenario-1).

technique. The MAVO-tuned FOPID controller performance improves by reducing the transient time to 1.758 seconds. The obtained value has a reduction of 82.4% compared to the PI controller and 63.32% compared to the PID controller.

Table 5. Comparison of transient response performances of diverse controllers (Scenario-1).

| Transient parameters | PSO-FOPID | WOA-FOPID | AVO-FOPID | MAVO-FOPID |
|---------------------------------------|-----------|-----------|-----------|------------|
| T_R (s) ($\times 10^{-5}$) | 3.709 | 3.289 | 2.957 | 2.905 |
| T_T (s) | 4.894 | 4.624 | 3.336 | 1.758 |
| T_S (s) | 9.998 | 9.996 | 9.981 | 9.573 |
| T_P (s) ($\times 10^{-1}$) | 7.162 | 1.557 | 1.453 | 1.383 |
| SSE ($\times 10^{-5}$) | 4.388 | 3.149 | 3.038 | 2.809 |
| CE (J) ($\times 10^{-1}$) | -0.058 | -0.042 | -0.051 | -0.049 |
| ITAE | 0.227 | 0.109 | 0.058 | 0.021 |
| ITSE ($\times 10^{-2}$) | 1.167 | 0.279 | 0.137 | 0.081 |
| IAE ($\times 10^{-1}$) | 1.799 | 0.957 | 0.682 | 0.461 |
| ISE ($\times 10^{-2}$) | 1.545 | 0.513 | 0.373 | 0.330 |
| $ P - O $ (p.u.) ($\times 10^{-1}$) | 1.555 | 0.780 | 0.775 | 0.759 |
| $ P - U $ (p.u.) | -0.128 | -0.132 | -0.134 | -0.139 |

B) Performance evaluation of the proposed FDVIDC strategy for RLP condition (Scenario-2)

A RLP scenario is considered with changes occurring every 20s from 0 to 100s. Fig. 12 shows the random load pattern. Fig. 13 depicts the frequency deviation of the IMG system under RLP conditions when optimized by different algorithms.

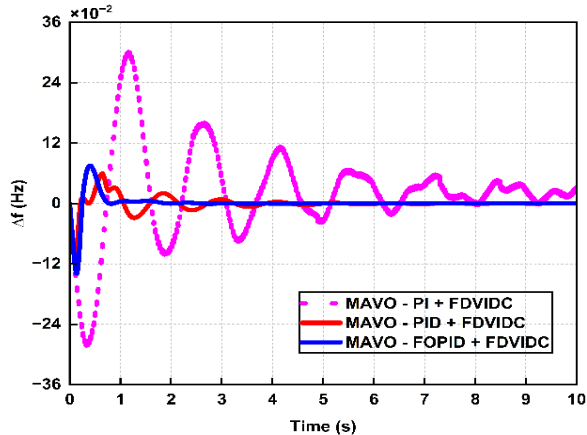


Fig. 12. RLP pattern.

The results indicate that the proposed MAVO algorithm minimizes frequency disparity with the shortest settling time

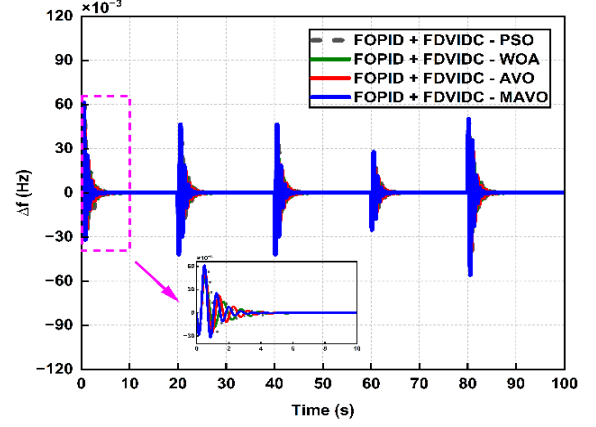


Fig. 13. System frequency response of the IMG with different algorithms (Scenario-2).

Table 6. Performance indices comparison of diverse algorithms (Scenario-2).

| Performance indices | ITAE | ITSE | IAE | ISE $\times 10^{-2}$ |
|---------------------|-------|-------|-------|----------------------|
| PSO-FOPID | 8.948 | 0.189 | 0.228 | 0.523 |
| WOA-FOPID | 7.926 | 0.162 | 0.197 | 0.418 |
| AVO-FOPID | 7.662 | 0.142 | 0.189 | 0.389 |
| MAVO-FOPID | 6.887 | 0.118 | 0.173 | 0.311 |

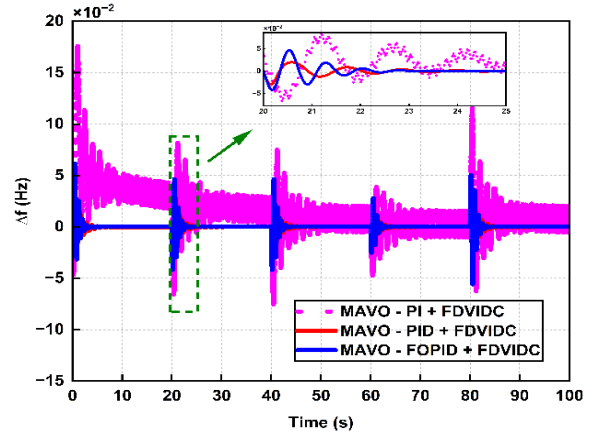


Fig. 14. System frequency response of the IMG with different controllers (Scenario-2).

before successive load disruptions, outperforming the AVO, WOA, and PSO-optimized FOPID controllers. Tables 6 and 7 display the different index values of scenario 2. In Table 6, the proposed MAVO-tuned FOPID controller shows the best performance with an ITAE value of 6.887. The obtained ITAE value is lower by 23.03%, 13.11%, and 10.12% than the values obtained using PSO, WOA, and AVO algorithms respectively.

The superior performance of the MAVO-optimized FOPID controller under sequential load disturbances is evident in Fig. 14. The results confirm that the selected FOPID controller effectively minimizes frequency oscillations, reduces settling time, and mitigates overshoot.

In Table 7, the proposed MAVO-tuned FOPID controller shows the best performance with an ITAE value of 5.392. The obtained ITAE value is lower by 92.36% and 29.21% than the values obtained using PI and PID controllers respectively.

Table 7. Performance indices comparison of diverse controllers (Scenario-2).

| Performance indices | ITAE | ITSE | IAE | ISE $\times 10^{-2}$ |
|---------------------|--------|-------|-------|----------------------|
| PI - MAVO | 70.640 | 2.007 | 2.030 | 8.253 |
| PID - MAVO | 7.617 | 0.193 | 0.189 | 0.490 |
| FOPID - MAVO | 5.392 | 0.069 | 0.136 | 0.179 |

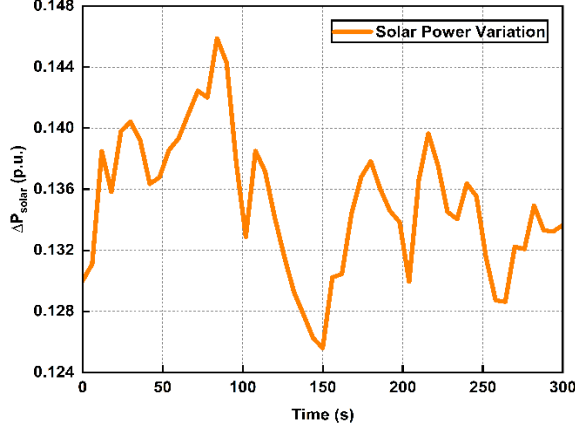


Fig. 15. Solar PV power variation.

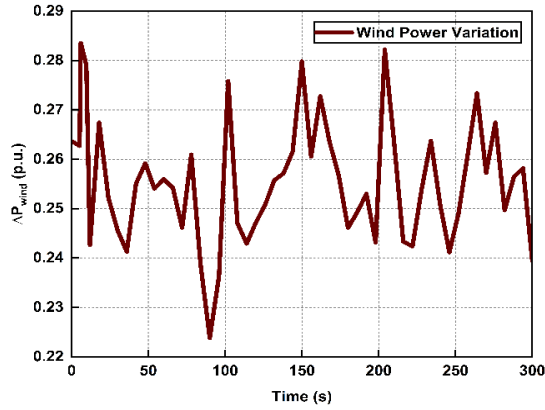


Fig. 16. Wind power variation.

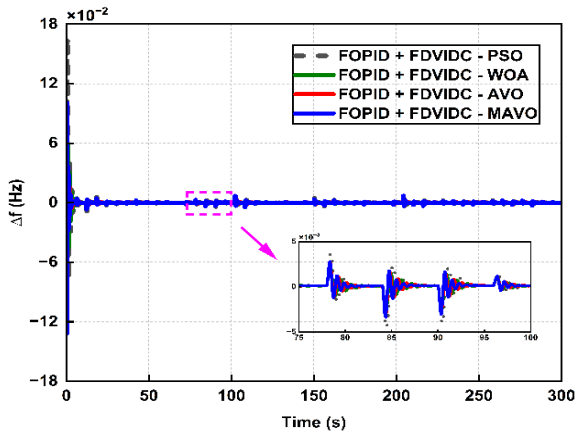


Fig. 17. System frequency response of the IMG with various algorithms (Scenario-3)

Table 8. Performance indices comparison of various algorithms (Scenario-3).

| Performance indices | ITAE | ITSE $\times 10^{-1}$ | IAE | ISE $\times 10^{-2}$ |
|---------------------|--------|-----------------------|-------|----------------------|
| PSO-FOPID | 19.070 | 0.461 | 0.315 | 1.636 |
| WOA-FOPID | 13.430 | 0.170 | 0.190 | 0.579 |
| AVO-FOPID | 12.880 | 0.157 | 0.163 | 0.431 |
| MAVO-FOPID | 12.220 | 0.149 | 0.155 | 0.422 |

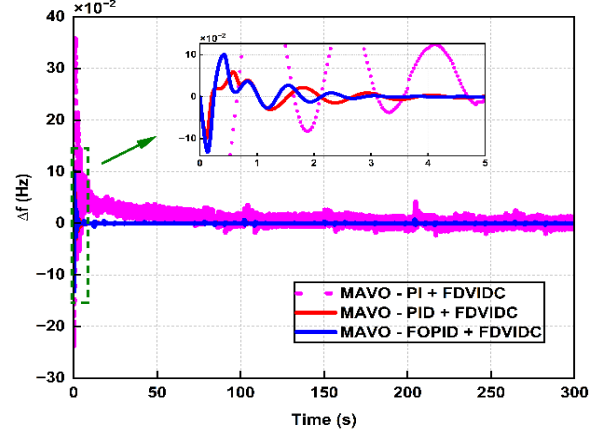


Fig. 18. System frequency response of various controllers (Scenario-3).

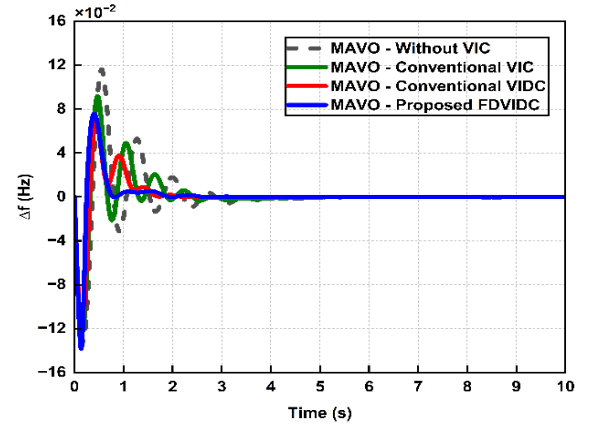


Fig. 19. Comparison curve of proposed FDVIDC strategy over conventional VIDC.

C) Performance evaluation of the proposed FDVIDC strategy for change in RESs (Scenario-3)

In this case, the proposed IMG network resilience is measured by adjusting the output power of the SPV and WTG units, as shown in Figs. 15 and 16, respectively.

Fig. 17 depicts the frequency variations of the IMG structure under diverse RES conditions using an FOPID controller tuned by various techniques. The findings show that the proposed MAVO algorithm successfully dampens frequency fluctuation with shorter settling times and lower overshoot values than the AVO, WOA, and PSO-tuned FOPID controllers. Tables 8 and 9 display the different index values of scenario 3.

In Table 8, the proposed MAVO-tuned FOPID controller shows the best performance with an ITAE value of 12.220. The obtained ITAE value is 35.92%, 9.01% and 5.12% smaller than ITAE values attained through PSO, WOA, and AVO techniques respectively. Fig. 18 depicts the dynamic behaviors of swings in RES power within the microgrid system. The FOPID controller outperforms conventional controllers under RES variations, reducing frequency

Table 9. Performance indices comparison of various controllers (Scenario-3).

| Performance indices | ITAE | ITSE $\times 10^{-1}$ | IAE | ISE $\times 10^{-2}$ |
|---------------------|---------|-----------------------|-------|----------------------|
| PI - MAVO | 371.700 | 51.450 | 4.096 | 18.860 |
| PID - MAVO | 12.050 | 0.091 | 0.189 | 0.459 |
| FOPID - MAVO | 8.395 | 0.015 | 0.153 | 0.423 |

Table 10. Transient parameters comparison of proposed FDVIDC with other VIC.

| Transient Parameters | Without VIC | Conventional VIC | Conventional VIDC | Proposed FDVIDC |
|----------------------|-------------|------------------|-------------------|-----------------|
| T_R (s) | 4.099 | 3.774 | 3.228 | 3.053 |
| $(\times 10^{-5})$ | | | | |
| T_T (s) | 3.937 | 3.239 | 1.907 | 1.750 |
| T_S (s) | 9.962 | 9.892 | 9.827 | 9.675 |
| T_P (s) | 1.741 | 1.557 | 1.428 | 1.322 |
| $(\times 10^{-1})$ | | | | |
| SSE | -3.148 | -4.162 | 3.769 | 4.385 |
| $(\times 10^{-5})$ | | | | |
| CE (J) | -0.070 | -0.068 | -0.063 | -0.049 |
| $(\times 10^{-1})$ | | | | |
| ITAE | 0.866 | 0.569 | 0.325 | 0.213 |
| $(\times 10^{-1})$ | | | | |

variation in overshoot value and settling time.

In Table 9, the proposed MAVO-tuned FOPID controller shows the best performance with an ITAE value of 8.395. The obtained ITAE value is lower by 97.74% and 30.33% than the values obtained using PI and PID controllers respectively.

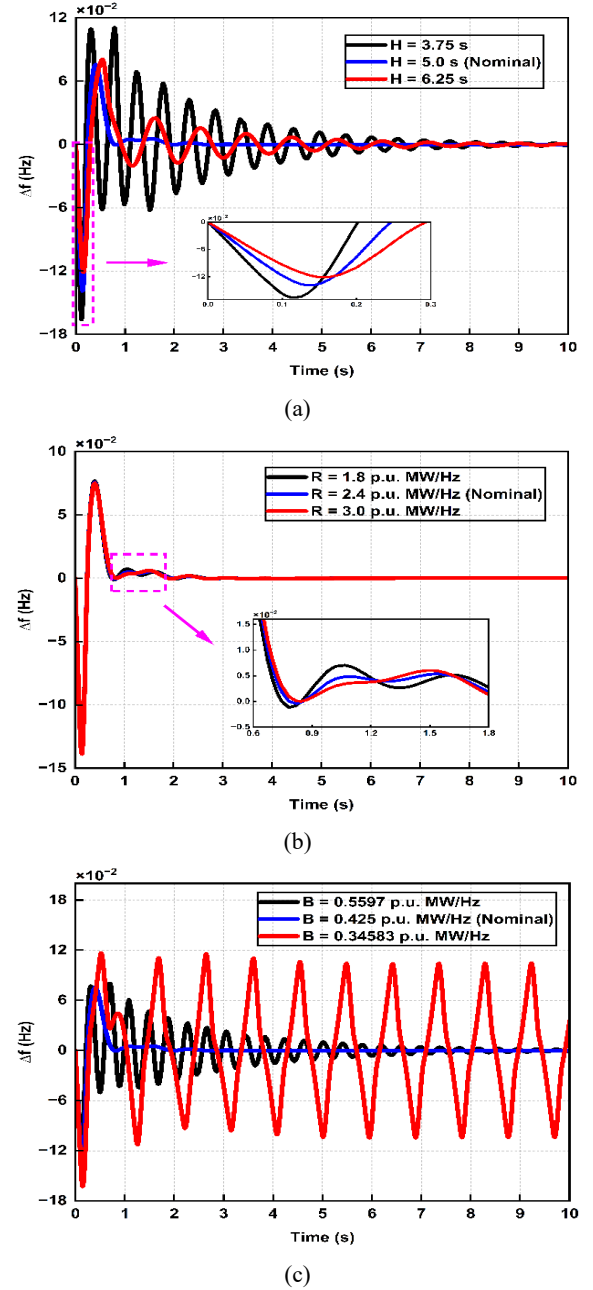
D) Investigations of the proposed FDVIDC strategy of the IMG network

The frequency deviation of the proposed FDVIDC strategy compared to previous VIC techniques for the IMG network is shown in Fig. 19. The comprehensive results show that the proposed FDVIDC techniques are better in several performance metrics listed in Table 10. The statistical data demonstrate that the MAVO-tuned FDVIDC approach excels in settling time, overshoots, control effort, undershoots, and other metrics.

In Table 10, the proposed FDVIDC strategy shows the best performance with an ITAE value of 0.213. The obtained ITAE value is lower by 75.4%, 62.56%, and 34.46% than those obtained without VIC, conventional VIC, and conventional VIDC techniques, respectively. In addition, Table 10 shows additional performance indices like ITSE, IAE, and ISE. The proposed MAVO-optimized FDVIDC parameters are lower than those of other comparison methods.

5.4. Robustness analysis

This study is conducted to assess the robustness (sensitivity) of the FOPID controller, which is fine-tuned using the proposed MAVO algorithm for the IMG network. This analysis considers variations in the IMG system parameters, specifically the system inertia constant (H), speed regulation (R), and frequency bias coefficient (B). Under nominal conditions, the system operates at 50% loading with H set to 5.0 seconds, R at 2.4 p.u. MW/Hz, and B at 0.425 p.u. MW/Hz. For the sensitivity study, each parameter is varied independently by $\pm 25\%$. At each altered condition, the FOPID controller is re-optimized using the MAVO algorithm to ensure adaptive tuning. The dynamic responses of the IMG system under these parameter shifts are depicted in Fig. 20. The results indicate that the MAVO-optimized FOPID controller maintains reliable and stable performance, even under significant system parameter variations.

Fig. 20. System frequency curve with change in system parameters (a) ΔH , (b) ΔR , (c) ΔB .

5.5. Stability analysis

This section presents the stability analysis of the IMG system controlled by the proposed MAVO-tuned FOPID controller. The system's dynamic behavior is represented in a state-space form derived from its fundamental differential equations using selected state variables. A detailed explanation of the state-space modeling process is available in Appendix B. The proposed IMG systems stability is examined in the time domain by evaluating its eigenvalues. As shown in Fig. 21, the eigenvalues are plotted on the complex plane, with color-coded points indicating their respective magnitudes. The system is considered stable if all eigenvalues lie in the left half of the complex plane, meaning their real parts are negative.

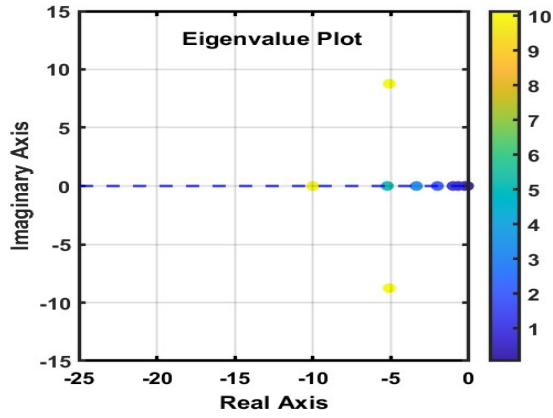


Fig. 21. Stability analysis of eigenvalue plot.

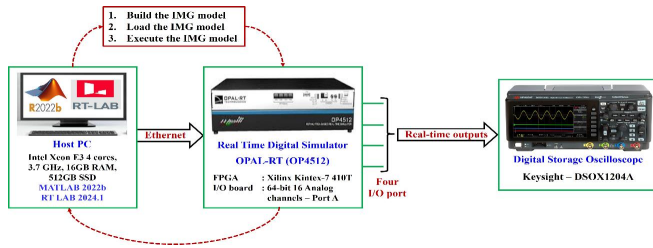


Fig. 22. HIL setup.

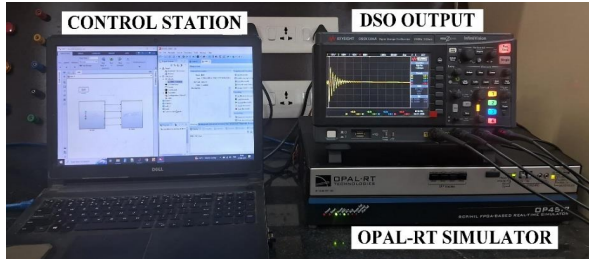


Fig. 23. OPAL-RT experimental setup.

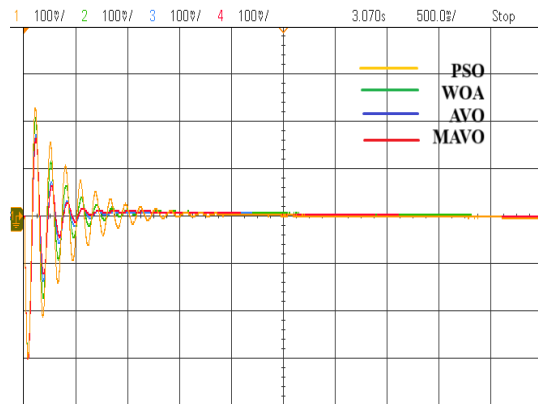


Fig. 24. OPAL-RT experimental result.

5.6. Real-time validation

To assess the real-time applicability of the MAVO-optimized FOPID controller, hardware-in-the-loop (HIL) testing is conducted using a real-time digital simulator (RTDS). The IMG model is initially developed in MATLAB/Simulink and compiled through

RT-LAB. It is then deployed on the OPAL-RT hardware platform for real-time execution. Fig. 22 illustrates the schematic layout of the HIL setup. In this configuration, a personal computer (PC) is utilized as the supervisory control unit, OPAL-RT is the primary real-time simulation engine, and a digital storage oscilloscope (DSO) is employed for real-time waveform monitoring and signal analysis.

Fig. 23 showcases the physical testbench of the HIL setup. The simulation operates at a fixed time step of $50 \mu s$ to ensure computational accuracy and system stability. Communication between the host PC and the OPAL-RT (OP4512) system is established via Ethernet, while analog input/output interfaces enable real-time signal exchange with external instruments, including the DSO (DSOX1204A). Signal conditioning and buffering are applied to maintain measurement fidelity. Additionally, predictive sampling and fixed-step numerical solvers are utilized to reduce latency and guarantee consistent real-time response. Detailed specifications of the real-time experimental setup used for validation are summarized in [26].

The IMG system is tested under an SLP scenario within the OPAL-RT environment, and the resulting frequency profiles are presented in Fig. 24. The outcomes demonstrate that the frequency deviations observed in the MATLAB simulations are in close agreement with those recorded by the real-time digital simulator.

6. CONCLUSION

This study introduces an innovative FDVIDC approach to deliver sufficient virtual inertia for enhancing the stability of an IMG system. An FOPID controller is utilized to manage the frequency dynamics of the biopower-based IMG network. The gain parameters for the FOPID controller and the newly proposed FDVIDC strategy are fine-tuned using a novel MAVO algorithm. Performance comparison indicates that MAVO surpasses traditional optimization methods like AVO, WOA, and PSO in minimizing the ITAE criterion. Furthermore, the FOPID controller demonstrates better dynamic behavior than conventional PI and PID controllers. The improvements in system stability and transient response offered by the FDVIDC method are evaluated against the traditional VIDC technique. Simulation outcomes validate the efficacy of the proposed framework, showing a 64.08% decrease in transient time, a 15.51% drop in control effort, and a 50.96% reduction in overshoot relative to existing LFC techniques documented in previous research.

Future work will involve the design of reinforcement learning-enabled AVO algorithms for frequency control in multi-microgrid architectures, along with integrating peer-to-peer energy trading frameworks.

APPENDIX A

BCHP: T_{BG} (Bio-Governor time constant) = 0.08 s, T_{BT} (Bio-Turbine time constant) = 0.3 s, K_{RT} (Bio-Reheat turbine gain) = 10.0, T_{RT} (Bio-Reheat turbine time constant) = 0.3 s. BDEG: K_{BA} (Valve actuator) = 1.0, T_{BA} (Actuator delay) = 0.2 sec, K_{BE} (Engine gain) = 1.0, T_{BE} (Engine time constant) = 1.0 s. RE Micropower sources: K_S & K_T (Solar field & Steam turbine gain) = 1.8 & 0.3, T_S & T_T (Solar field & Steam turbine time constant) = 1.0 s & 1.0 s, K_{WTG} & T_{WTG} (Wind turbine gain & time constant) = 1.0 & 1.5 s, K_{AE} & T_{AE} (Aqua Electrolyzer power gain & time constant) = 0.002 & 0.5 s, K_{FC} & T_{FC} (Fuel cell power gain & time constant) = 0.002 & 4.0 s. HESS: K_{BES} & T_{BES} (BES gain & time constant) = 1.0 & 0.1 s, K_{FES} & T_{FES} (FES gain & time constant) = 1.0 & 0.1 s. MAVO algorithm parameters: $P_1 = P_2 = 0.3$, $P_3 = 0.4$, $L_1 = 0.8$, $L_2 = 0.2$, $W = 2.5$.

APPENDIX B

The proposed IMG network state-space representation is given as follows:

$$\dot{X} = AX + B_1u + B_2W \quad (30)$$

$$Y = CX \quad (31)$$

Here, A is the state matrix represented as:

$$\begin{bmatrix} a_{11} & a_{12} & \cdots & a_{1,24} \\ a_{21} & a_{22} & \cdots & a_{2,24} \\ \vdots & \vdots & \ddots & \vdots \\ a_{24,1} & a_{24,2} & \cdots & a_{24,24} \end{bmatrix} \quad (32)$$

The vector form of state variables (X) are as follows:

$$X = [X_1, X_2, X_3, \dots, X_{24}]^T \quad (33)$$

Now, the state space variables along with the IMG network parameters are denoted as:

$$\begin{aligned}
X = & \\
& [\Delta f, \Delta P_{\text{BCHP}}, \Delta P_{\text{RT}}, \Delta P_{\text{BG}}, \Delta P_{\text{BDEG}}, \Delta P_{V1}, \\
& \Delta P_{\text{BCHP}}, \Delta P_{\text{RT}}, \Delta P_{\text{BG}}, \Delta P_{\text{BGTG}}, \Delta P_{\text{CR}}, \Delta P_{\text{SBG}}, \\
& \Delta P_{\text{STPG1}}, \Delta P_{\text{SO1}}, \Delta P_{\text{STPG2}}, \Delta P_{\text{SO2}}, \Delta P_{\text{WTPG1}}, \Delta P_{\text{WTPG2}}, \\
& \Delta P_{\text{WTPG3}}, \Delta P_{\text{AE}}, \Delta P_{\text{FC1}}, \Delta P_{\text{FC2}}, \Delta P_{\text{FDVIDC}}]^T
\end{aligned} \tag{34}$$

The disturbance signals (W) considered in the IMG system can be formulated as:

$$W = [\Delta P_{Solar}, \Delta P_{Wind}, \Delta P_L]^T \quad (35)$$

The control signals (u) are given as:

$$u = [\Delta P_{\text{FOPID}}, \Delta P_{\text{FDVIDC}}]^T \quad (36)$$

The output matrix (Y) of the IMG network can be represented as:

The thorough state-space representation study discussed above is based on the IMG network. The system's stability is determined by evaluating the eigenvalues derived from the system matrix A .

$$Y = [1000000000000000000000000]^T X^T \quad (37)$$

REFERENCES

- [1] D. Chong, Z. Tian, H. Yan, Z. Sha, Z. Wang, and Q. Zhao, "Coordination optimization within large-scale virtual power plant for frequency stability improvement under internal power and external frequency fluctuations," *Appl. Energy*, vol. 384, p. 125416, 2025.
- [2] D. del Giudice, A. Brambilla, S. Grillo, and F. Bizzarri, "Effects of inertia, load damping and dead-bands on frequency histograms and frequency control of power systems," *Int. J. Electr. Power Energy Syst.*, vol. 129, p. 106842, 2021.
- [3] H. Nerkar, P. Kundu, and A. Chowdhury, "An analysis of the impact on frequency response with penetration of res in power system and modified virtual inertia controller," *J. Oper. Autom. Power Eng.*, vol. 11, no. 1, pp. 39–49, 2023.

- [4] I. Alotaibi and M. M. Abido, "Robust h_{∞} based virtual synchronous generators for low inertial microgrids considering high penetration of renewable energy," *IEEE Trans. Ind. Appl.*, 2024.
- [5] T. Kerdphol, F. S. Rahman, M. Watanabe, and Y. Mitani, "Robust virtual inertia control of a low inertia microgrid considering frequency measurement effects," *IEEE Access*, vol. 7, pp. 57550–57560, 2019.
- [6] A. M. Mohan, N. Meskin, and H. Mehrjerdi, "Mpc-based virtual inertia control of islanded microgrid load frequency control and dos attack vulnerability analysis," in *Proc. SGRE 2022*, IEEE, 2022.
- [7] H. Ali *et al.*, "A new frequency control strategy in an islanded microgrid using virtual inertia control-based coefficient diagram method," *IEEE Access*, vol. 7, pp. 16979–16990, 2019.
- [8] A. Altaf, M. Kumar, D. Biswas, R. Mahadeva, and S. P. Patole, "Virtual inertia controller design based on mixed sensitivity constraint h_{∞} approach for load frequency regulation of islanded ac microgrid," *IEEE Access*, vol. 12, pp. 102328–102336, 2024.
- [9] H. E. A. Abbou *et al.*, "Accelerating virtual rotor control with integral feedback loop in low-inertia microgrids," *Int. J. Electr. Power Energy Syst.*, vol. 162, p. 110253, 2024.
- [10] M. Chang, M. Salem, and F. A. Mohamed, "Adaptive virtual inertia emulation based on policy gradient clipping for low-inertia microgrids with phase-locked loop dynamics," *Comput. Electr. Eng.*, vol. 125, p. 110477, 2025.
- [11] R. K. Khadanga, D. Das, A. Kumar, and S. Panda, "Sine augmented scaled arithmetic optimization algorithm for frequency regulation of a virtual inertia control based microgrid," *ISA Trans.*, vol. 138, pp. 534–545, 2023.
- [12] H. Shayeghi and A. Rahnama, "Frequency regulation of a standalone interconnected ac microgrid using innovative multistage tdf(1+fopi) controller," *J. Oper. Autom. Power Eng.*, vol. 12, no. 2, pp. 121–133, 2024.
- [13] V. Rajaguru and K. I. Annappoorani, "Virtual synchronous generator based superconducting magnetic energy storage unit for load frequency control of micro-grid using african vulture optimization algorithm," *J. Energy Storage*, vol. 65, p. 107343, 2023.
- [14] S. E. Sati, A. Al-Durra, H. Zeineldin, T. H. M. EL-Fouly, and E. F. El-Saadany, "A novel virtual inertia-based damping stabilizer for frequency control enhancement for islanded microgrid," *Int. J. Electr. Power Energy Syst.*, vol. 155, p. 109580, 2024.
- [15] T. K. Roy and A. M. T. Oo, "Virtual inertia and damping-based cascaded control approach for enhancing load frequency control in low-inertia multi-area power systems," *J. Eng.*, vol. 2025, no. 1, 2025.
- [16] S. Das, S. Datta, and L. C. Saikia, "Effect of pi-ti-based virtual inertia controller with virtual damping on a renewable energy-based multi-area power system under deregulation," *Arab. J. Sci. Eng.*, vol. 48, no. 5, pp. 6431–6452, 2023.
- [17] R. K. Khadanga, D. Das, A. Kumar, and S. Panda, "An improved parasitism predation algorithm for frequency regulation of a virtual inertia control based ac microgrid," *Energy Sources A: Recovery Util. Environ. Eff.*, vol. 44, no. 1, pp. 1660–1677, 2022.
- [18] M. Sajadinia, "An adaptive virtual inertia control design for energy storage devices using interval type-2 fuzzy logic and fractional order pi controller," *J. Energy Storage*, vol. 84, p. 110791, 2024.
- [19] S. K. Bhagat, L. C. Saikia, N. R. Babu, and D. Saha, "Impact of pll and virtual inertia on deregulated agc system integrated with parallel ac/hvdc," *IETE J. Res.*, vol. 69, no. 5, pp. 2514–2527, 2023.
- [20] S. Oshnoei, M. R. Aghamohammadi, S. Oshnoei, S. Sahoo, A. Fathollahi, and M. H. Khooban, "A novel virtual inertia

- control strategy for frequency regulation of islanded microgrid using two-layer multiple model predictive control,” *Appl. Energy*, vol. 343, p. 121233, 2023.
- [21] T. Kerdphol, M. Watanabe, K. Hongesombut, and Y. Mitani, “Self-adaptive virtual inertia control-based fuzzy logic to improve frequency stability of microgrid with high renewable penetration,” *IEEE Access*, vol. 7, pp. 76071–76083, 2019.
- [22] G. Magdy, H. Ali, and D. Xu, “A new synthetic inertia system based on electric vehicles to support the frequency stability of low-inertia modern power grids,” *J. Clean Prod.*, vol. 297, p. 126595, 2021.
- [23] M. H. Norouzi, A. Oshnoei, B. Mohammadi-Ivatloo, and M. Abapour, “Learning-based virtual inertia control of an islanded microgrid with high participation of renewable energy resources,” *IEEE Syst. J.*, vol. 18, no. 2, pp. 786–795, 2024.
- [24] B. Yildirim, M. Gheisarnejad, A. Mohammadzadeh, and M. H. Khooban, “Intelligent frequency stabilization of low-inertia islanded power grids-based redox battery,” *J. Energy Storage*, vol. 71, p. 108190, 2023.
- [25] W. M. Hamanah, M. Shafiullah, L. M. Alhems, M. S. Alam, and M. A. Abido, “Realization of robust frequency stability in low-inertia islanded microgrids with optimized virtual inertia control,” *IEEE Access*, vol. 12, pp. 58208–58221, 2024.
- [26] S. P. and R. S. M. M. M., “Chaotic african vultures optimization based non-linear fopid controller for frequency regulation in standalone microgrid system,” *Eng. Res. Express*, 2025.
- [27] B. A. Fadheel *et al.*, “Optimal tuning of virtual inertia control for frequency regulation of microgrid,” *IEEE Can. J. Electr. Comput. Eng.*, vol. 47, no. 2, pp. 60–69, 2024.
- [28] S. Palaniyappan and M. M. R. Singaravel, “Integration of vanadium redox battery for virtual inertia supported load frequency control of islanded microgrid system,” in *2023 IEEE Int. Conf. Power Electron. Smart Grid Renewable Energy*, IEEE, 2023.
- [29] S. Palaniyappan and M. M. R. Singaravel, “Opposition african vultures optimization based nfopid controller for frequency stabilization of multi-microgrid network,” *Comput. Electr. Eng.*, vol. 122, p. 109959, 2025.
- [30] H. Shayeghi, A. I. Rahnama, and H. Mojarad, “Designing a multi-objective optimized parallel process controller for frequency stabilization in an islanded microgrid,” *J. Oper. Autom. Power Eng.*, 2022.
- [31] S. Palaniyappan and M. M. R. Singaravel, “Agc of a multi-area power system interconnected by ac/dc links with redox flow battery,” in *4th Int. Conf. Energy Power Environ.*, IEEE, 2022.
- [32] B. Abdollahzadeh, F. S. Gharehchopogh, and S. Mirjalili, “African vultures optimization algorithm: A new nature-inspired metaheuristic algorithm for global optimization problems,” *Comput. Ind. Eng.*, vol. 158, 2021.
- [33] Q. Wang, Y. Li, Z. Hou, J. Zou, and J. Zheng, “A novel multi-population evolutionary algorithm based on hybrid collaboration for constrained multi-objective optimization,” *Swarm Evol. Comput.*, vol. 87, p. 101581, 2024.